Numerical Prediction of Aerofoil Aerodynamics at Low Reynolds number for MAV Application

A. Abdul Huq, R. Anand Sankar, C. Lakshmanan, C. Rukesh
D. S. Kulkarni, M.B.Subramanya, B.N.Rajani

NAL PD 0910

Computational & Theoretical Fluid Dynamics Divisison
National Aerospace Laboratories, Bangalore 560 017

June 2009

Contents

1 Introduction

1.1 Background

Low Reynolds number aerodynamics are important for both natural and man-made flying objects. The complexity of the aerodynamics and flight of small birds, bats, insects has generated enormous research interest among biologists and aerospace engineering community. Over last few decades there is a growing interest in designing aircraft that are as small as possible for special military and civil missions. Many such aircraft are currently under development among them are the Micro Air Vehicle (MAV) which have received special attention for both civil and military application. MAVs are unmanned autonomous flying machines with linear dimension of 15cm, gross take-off weight of approximately 100g carrying a payload of 20g and the expected loiter time is of the order of 60 minutes. Two important challenging problems in design of MAV are (i) low Reynolds number (Re), which results in unfavourable aerodynamic conditions to support controlled flight, and (ii) small physical dimensions, resulting in certain favorable scaling characteristics including structural strength, reduced stall speed, and low inertia. MAVs generally fly in the Reynolds number ranging from 1000 to 1,20,000 (low Reynolds number regime), whereas for the full size helicopoters and aeroplanes the Reynolds number is around 10^7. The growing interest in MAV and its aerodynamic challenges has created the need for improved understanding of the aerodynamics and related flow physics. Aerodynamic designs of MAVs, reported so far, have employed different kind of efficient lift generation systems viz., fixed wing [1, 2, 3], flapping wings [4], flexible wing [5, 6] and rotary wings [7, 8, 9] or their combinations. The fixed-wing MAVs usually fly at the upper end of the low Reynolds number regime *i.e.* around 10^5 [10], rotary wing generally fly at Reynolds number ranging from 20,000 to 70,000. and flapping wing fly at Reynolds number ranging from 1,000 to 10,000 in which the viscous effect is expected to be prominant.

Fixed wing MAVs are simple and easy to implement. The aerodynamic performance is known to deteriorate when the operating Reynolds number is less than 10^5. The poor performance at low Reynolds number is mainly because the flow separates at a relatively low angle of attack. This early laminar separation is often formed on the upper surface of the aerofoil, leading to a lower lift to drag ratio, with a delayed stall angle. Therefore the selection of aerofoil plays a key role in the designing of MAV wings. The most commonly used low Reynolds number aerofoil sections are NACA, Wortman, Althaus, Selig, Eppler, MH, Drela and Zimmerman.

Recently, National Aerospace Laboratories (CSIR) and Aeronautical Development Establishment (DRDO) have initiated a joint effort to design and develop a fixed wing MAV in the next two years and eventually demonstrate the technology developed in a flying unit with pre-defined mission. To fulfill this mission CFD analysis of thin aerofoil sections and wings are required to be carried out in order to understand the aerodynamic performance of thin aerofoil at low Reynolds numbers and design a suitable wing configuration.

The present study is to understand the aerodynamic characteristics of NACA aerofoil sections at a low

Reynolds number of 87000 for different geometrical parameters *viz.*, thickness, camber and location of maximum camber.

1.2 Scope of the present work

The Current work will be mainly focused on the two-dimensional numerical simulation of different aerofoil sections to study their relative performance in terms of the lift-to-drag ratio. The parameter investigated will be mainly on the thickness, camber and the location of maximum camber for NACA series at a chord based flow Reynolds number, $Re = 87,000$. The two-dimensional analysis will be carried out using the in-house multiblock structured flow solution algorithm RANS3D [11, 12, 13, 14]. The RANS3D code developed at CTFD division NAL, Bangalore, is based on an implicit finite volume algorithm to solve the time-averaged Navier Stokes equations for unsteady incompressible turbulent flow with moving boundaries in an inertial frame of reference. The RANS3D code has been validated extensively for variety of low speed internal and external turbulent flow application problems.

The flow code is coupled to an appropriate pre-processor for generation of boundary fitted curvilinear grid around the aerofoil and a post-processing interface for numerical visualization of the flow and calculation of the aerodynamic coefficeints.

1.3 Documentation outline

The present document consists of five different sections starting with this introduction as the first one. Section 2 describes in brief the grid generation procedure for the body-fitted grid around the aerofoil. The mathematical modelling of equations of turbulent fluid motion is described in Section 3. Results on turbulent flow past various 4 digit NACA aerofoil sections for flow Reynolds number of 87,000 at different angles of attack varying from 0° to the stall angle are discussed in Section 4, followed by few important concluding remarks and the scope of future work in Section 5.

2 Numerical grid generation procedure

Generation of smooth, body-fitted grids with approximate orthogonality at the boundaries is practically the first step towards the accurate numerical solution of fluid flow equations for arbitrary configuration, using finite volume, finite element and similar methods. The location and kind of physical boundaries, interpreted mathematically as the boundary conditions of the governing differential equations of flow determine the spatial distribution of the flow variables in the domain of interest. Therefore the distribution of grid points on domain boundaries, usually specified by the user, should accurately reflect the geometrical boundaries of the domain. The grid should also have sufficient number of points distributed appropriately to detect the major characteristics of the flow. Other desirable features of a good grid generation methodology are the smoothness and the boundary-orthogonality of the grid generated, an easy and direct control of grid-spacing and grid skewness at any desired location and finally an efficient and fast numerical algorithm. A poorly constructed grid may yield inaccurate results and may bring down the convergence rate of the numerical solution of the flow equations also to a prohibitively low level.

2.1 Differential-algebraic Hybrid method for two dimensional plane

The present grid generation algorithm [15] developed at the CTFD Division, NAL involves the solution of the elliptic type differential equations at a coarse level, followed by simple algebraic interpolation from the coarse to a finer level. The coarse grid is primarily generated by solving a system of inverted Poisson equations for a given point distribution at all four boundaries of a two dimensional computation domain. The control functions in the equations are automatically adjusted in an iterative procedure to achieve boundary-orthogonality and need no ad-hoc adjustment of the problem-dependent parameters. Finally, when the desired concentration of grid points is specified at the fine level on one boundary along each direction, the fine level field grid coordinates is obtained by fitting Bicubic Spline functions passing through the coarse level grid nodes. This Hybrid approach proposed first by Zhu [16] makes a compromise between the simple algebraic and the expensive differential approach and guarantees smooth grid of desired fineness and approximate boundary-orthogonality for a very reasonable computation cost.

2.2 Typical O-grid topology around an aerofoil

The present flow computation has been carried out using O- topology for the different NACA series aerofoil analysed. Figs. 2.1 and 2.2 show the typical 2-block O-grid topology around a symmetric (NACA0002) and cambered (NACA4402) aerofoil with the zoomed views near the leading and trailing edge of the aerofoil where the fine resolution near the important areas of the domain are clearly demonstrated. For the present O-grid topology, the cut line at the block interface is chosen to be a vertical line passing through the mid-chord point of the aerofoil and the far field boundary is circular

at a radius of $15C$, where C is the chord of the aerofoil. Near the aerofoil surface, the grid lines are specially stretched along the wall-normal direction in order to have a better resolution of the steep flow variable gradients in the boundary layer. Number of grid nodes used along circumferential direction is 321 and the number of nodes along radial direction is 101 in each block of the O-grid with one overlapping control volume on either side all along the cut line. The advantage of the O-grid is that one may use better resolution of the aerofoil surface since all the nodes along circumferential direction are covered on one J= constant line.

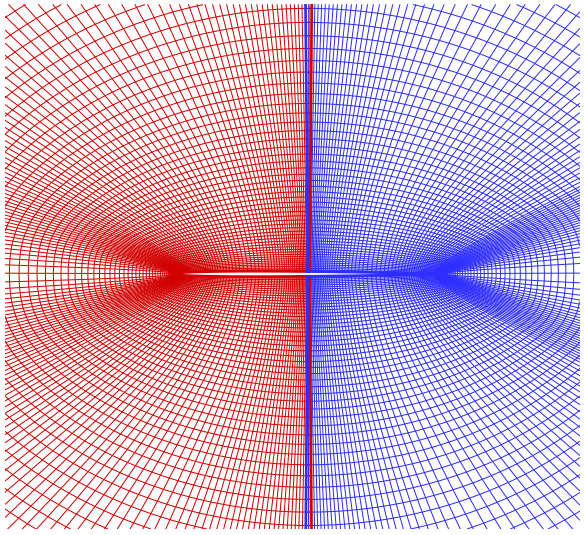

(a) Zoomed view of flow domain

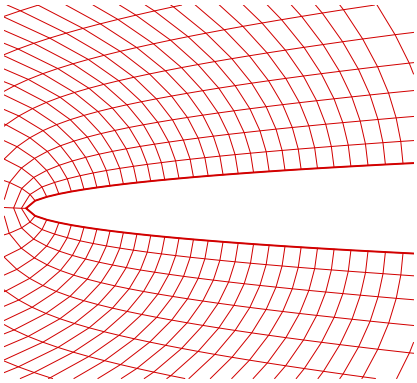

(b) Zoomed view near leading edge

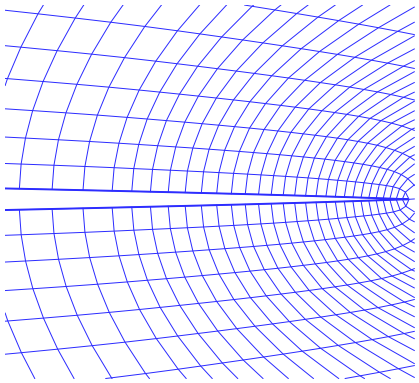

(c) Zoomed view near trailing edge

Figure 2.1: Multiblock grid (321×101) around NACA0002 aerofoil

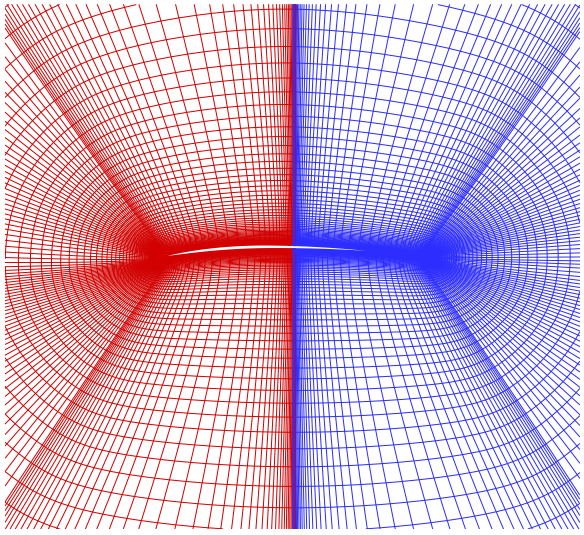

(a) Zoomed view of flow domain

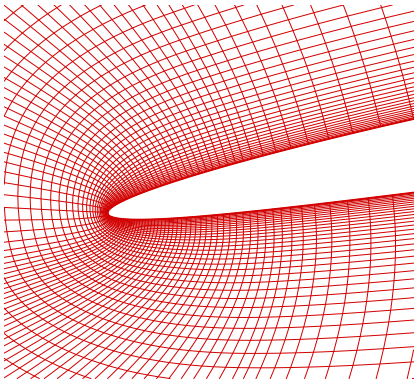

(b) Zoomed view near leading edge

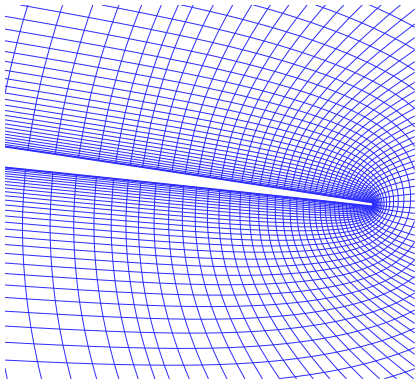

(c) Zoomed view near trailing edge

Figure 2.2: Multiblock grid (321×101) around NACA4402 aerofoil

3 Mathematical Modelling of Flow Physics

3.1 Introduction

The analysis of flow around different aerofoil sections is carried out in this work through numerical solution of the relevant Navier Stokes (NS) equation system for unsteady two dimensional flows. The numerical simulation of the NS equation needs an appropriate mathematical model which can handle the geometrical complexities like arbitrary shaped boundaries as well as the physical complexities like simulating the effects of turbulence. The basic equations to be solved are a set of non-linear, strongly coupled partial differential equations representing the conservation of mass and three momentum components along the cartesian direction.

3.2 Governing equations for instantaneous fluid flow

The present pressure-based finite volume algorithm uses non-orthogonal coordinates with cartesian velocities as dependent variables with the NS equations written in an inertial frame of reference. In this generalized coordinate system with moving boundaries, the governing equations for conservation of mass and momentum for instantaneous fluid motion for incompressible flow can be written as follows :

Momentum transport for the Cartesian velocity component U_i:

$$\frac{\partial(\rho U_i)}{\partial t} + \frac{1}{J}\frac{\partial}{\partial x_j}\left[(\rho U_i(U_k - \dot{x}_k)\beta_k^j)\right] - \frac{\mu}{J}\left[\frac{\partial U_i}{\partial x_m}B_m^j + \frac{\partial(U_k - \dot{x}_k)}{\partial x_m}\beta_i^m\beta_j^k\right] + p\beta_i^j = S_{U_i} \qquad (3.1)$$

where, J is the transformation Jacobian between cartesian and the curvilinear coordinates, β_j^i and B_j^i are the relevant geometric coefficients related to the transformation, p is the pressure, μ is the fluid viscosity and ρ is the fluid density. j, k and m are used as repeated summing indices along the three grid directions. U_k is the mean Cartesian velocity solved for along the 'k' -direction, $\dot{x}_k$ is the grid velocity along the k-direction and S_{U_i} is any other body forces appearing as source terms. These momentum equations are further supplemented by the mass conservation or the so-called continuity equation which, for incompressible flows, is just a kinematic constraint on the velocity field.

Mass Conservation (Continuity):

$$\frac{\partial}{\partial x_j}\left[\rho(U_k - \dot{x}_k)\beta_k^j\right] = 0 \tag{3.2}$$

Analysis of any 3D unsteady flow situation requires the solution of the three non-linear strongly coupled partial differential equations, given by Eqs. 3.1 and 3.2 (the three momentum equations for the three cartesian velocity components U_k, k = 1, 2 and 3 and the continuity) for the four unknowns *viz.*, U_1, U_2 U_3 and *p*. The grid velocity components, $\dot{x}_k$ for $k = 1, 2, 3$ are zero for the present analysis. The details of the finite volume formulation, the initial and boundary conditions for the flow past an aerofoil and the numerical solution procedure are provided in the following sections. For the present analysis 2D simulations have been carried out by ingorning the effect due to the third direction which will be described in Section 4.1.2.

3.3 Unsteady Reynolds Averaged Navier Stokes (URANS) Equations

In this approach, the Reynolds averaging concept, illustrated in Fig. 3.1, is directly used to replace the instantaneous flow variables (Eqs. 3.1 and 3.2) by the so-called Time-Averaged variables or Phase-Averaged variables for the steady and time-dependent mean flow situations respectively. The only assumption in this representation is that the time scale of the mean flow variation is quite large compared to the time scale of the turbulent fluctuations.

3.3.1 Basic Concept of Averaging for Turbulent Flows

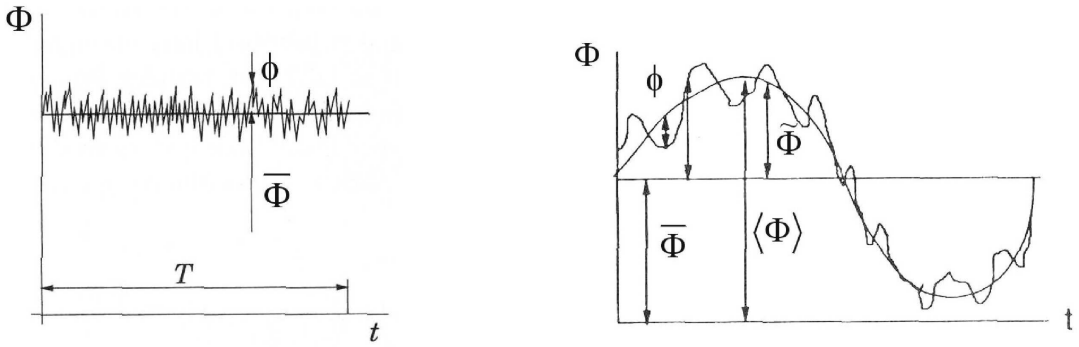

Figure 3.1: Statistical averaging for turbulent flow

The concept of averaging is clearly explained based on the time record of any variable Φ (Fig. 3.1). In case of stationary turbulence, shown in Fig. 3.1(a), the averaged variable $\bar{\Phi}$ does not change with time whereas only the turbulent fluctuations (ϕ) are function of time and hence the mean flow is designated

as a steady flow. For stationary turbulence flows, the instantaneous flow variables using the Reynolds decomposition can be written as follows

$$\Phi = \bar{\Phi} + \phi \;\text{ where }\; \bar{\Phi} = \lim \frac{1}{T}\int_0^T \Phi dt \tag{3.3}$$

For solving the steady turbulent flow equations, the time averaged flow variables $(\bar{\Phi})$ are solved and the turbulent fluctuations (ϕ) are simulated through turbulence models. On the other hand in Fig. 3.1(b), the instantaneous value of Φ consists of three different components - the time averaged $(\bar{\Phi})$, the coherent $(\tilde{\phi})$ and the turbulent fluctuations (ϕ) where the last one is the effect of the randomness of turbulence and hence stochastic in nature and coherent part however is deterministic. Using the Reynolds decomposition, the instantaneous flow variables for unsteady or periodic turbulent flow situation can be written as

$$\Phi = \langle\Phi\rangle + \phi \text{ where } \langle\Phi\rangle = \bar{\Phi} + (\tilde{\phi}) \tag{3.4}$$

and the time-dependent phase averaged flow variables are $(\langle\Phi\rangle)$ solved and the stochastic (turbulent fluctuations) part is simulated through turbulence models. Substituting the instantaneous flow variable in the instantaneous Navier-Stokes equation (Eqs. 3.1 and 3.2) according to the Reynolds decomposition (Eq. 3.4) and averaging the equation, the RANS equations for unsteady turbulent incompressible flow in *non-orthogonal curvilinear coordinates* with cartesian velocities as dependent variables may be written in a compact form as follows:

Momentum transport for the Cartesian velocity component $\langle U_i\rangle$:

$$\frac{\partial\left(\rho\langle U_i\rangle\right)}{\partial t} + \frac{1}{J}\frac{\partial}{\partial x_j}\left[\rho\langle U_i\rangle(\langle U_k\rangle - \dot{x}_k)\beta_k^j - \frac{\mu}{J}\left(\frac{\partial\langle U_i\rangle}{\partial x_m}B_m^j + \frac{\partial(\langle U_k\rangle - \dot{x}_k)}{\partial x_m}\beta_i^m\beta_k^j\right)\right] + \frac{1}{J}\frac{\partial}{\partial x_j}\left[\langle P\rangle\beta_i^j + \rho\langle u_i u_j\rangle\beta_k^j\right] = S_{U_i} \tag{3.5}$$

where, $\langle P\rangle$ is the phase averaged pressure, $\langle U_i\rangle$ is the phase averaged velocity component solved for and $-\rho\langle u_i u_j\rangle$ is the turbulent stress term appearing as correlation between the unknown fluctuating velocity components $u_i \; and \; u_j$. $\dot{x}_i$ is the grid velocity component which is zero for this analyses. These momentum equations are further supplemented by the mass conservation or the so-called continuity equation.

Mass Conservation (Continuity):

$$\frac{\partial}{\partial x_j}\left(\rho\langle U_k - \dot{x}_i\rangle\beta_k^j\right) = 0 \tag{3.6}$$

However Eq. 3.5 and Eq. 3.6 do not form a closed system due to the presence of the unknown turbulent stress term $-\rho\langle u_i u_j\rangle$.

3.4 Turbulence Modelling

3.4.1 Eddy Viscosity hypothesis

The task of the turbulence model is to provide a means for calculating the turbulent stresses appearing in the Reynolds-Averaged equations. In Eddy Viscosity based models where the turbulent stress is expressed in terms of the mean velocity gradients as following:

$$-\rho\langle u_i u_j\rangle = \mu_t\left(\frac{\partial\langle U_i\rangle}{\partial x_j}+\frac{\partial\langle U_j\rangle}{\partial x_i}\right)-\frac{1}{3}\rho\delta_{ij}\langle u_k u_k\rangle \tag{3.7}$$

where, $\langle U_i\rangle$ is the phase-averaged velocity, u_i is the corresponding fluctuating component, ρ is the density, δ_{ij} is the Kronecker Delta and *k* is the summation index over $k = 1, 2, 3$. The term $\frac{2}{3}\rho k\delta_{ij}$ only ensures that the sum of the normal stresses is *2k* as per definition of *k* , the turbulence kinetic energy $k = \frac{1}{2}\overline{u_i u_j}$. The eddy viscosity μ_t is assumed to be an isotropic scalar quantity whose value depends on the local state of turbulence. Substituting the turbulent stress term in Eq. 3.5 and carrying out some algebraic manipulation one may rewrite the mean momentum equation as following :

$$\frac{\partial\left(\rho\langle U_i\rangle\right)}{\partial t}+\frac{1}{J}\frac{\partial}{\partial x_j}\left[\left(\rho\langle\langle U_i\rangle(\langle U_k\rangle-\dot{x}_k)\rangle\beta_k^j\right)-\frac{(\mu+\mu_t)}{J}\left(\frac{\partial\langle U_i\rangle}{\partial x_m}B_m^j+\frac{\partial\langle U_k\rangle}{\partial x_m}\beta_i^m\beta_k^j\right)\right] + \frac{1}{J}\frac{\partial}{\partial x_j}\left[\langle P\rangle\beta_i^j\right]=S_{U_i} \tag{3.8}$$

The algebraic or zero equation turbulence models [17, 18], employed very successfully for attached boundary layer type flows, compute the eddy viscosity (μ_t) at any field point as an algebraic function of the mean velocity gradients and the normal distance from the solid surface. These models are computationally cheap but sometimes call for complicated interpolations to determine the normal distance from wall for highly skewed grids near the body surface and cannot, in general, simulate separated flows. On the other hand for one or two equation eddy viscosity based turbulence models, transport equation are solved for one or more turbulence scalars. For the present study the SST model has been used to simulate the effect of turbulence which is described briefly in following subsection.

3.4.2 SST model

The idea behind Shear Stress Transport (SST) model is to retain the robust and accurate formulation of Wilcox $k-\omega$ [19] in the near wall region, and to take advantage of the free stream independence of the $k-\epsilon$ model [20] in the outer part of the boundary layer. To achieve this, the $k-\epsilon$ model is first transformed into a $k-\omega$ formulation. The difference between this formulation and the original $k-\omega$ model is that when ϵ is replaced in its original transport equation of turbulent kientic energy as $\epsilon = \omega k$, an additional cross-diffusion term appears in the ω-form of the equation and of course with different modelling constants. The equations of the original $k-\omega$ model is then multiplied

by a blending function F_1 and the transformed $k-\epsilon$ model equations by a function $(1-F_1)$ and the addition of the two transformed equations form a linear combination of $k-\omega$ model near wall $(F_1=1)$ and $k-\epsilon$ model near the far field $(F_1=0)$. In this model the turbulent or eddy viscosity, μ_t, is evaluated in the following way using a limiter based on mean vorticity Ω and another damping function F_2

$$\mu_t = \frac{\rho a_1 k}{max(a_1\omega, \Omega F_2)} \tag{3.9}$$

where k is the turbulence kinetic energy and ω is the specific dissipation rate which are evaluated spatially by solving the following transport equations. The above limiter has been validated for many adverse pressure gradient flow situations and has been found to be more accurate than the parent models based on $k-\epsilon$ or $k-\omega$ only.

k**- equation**

$$\frac{\partial(\rho k)}{\partial t} + \frac{1}{J}\frac{\partial}{\partial x_j}\left[(\rho\langle U_j - \dot{x_k}\rangle\beta_k^j k) - \frac{(\mu+\mu_t/\sigma_k)}{J}\left(\frac{\partial k}{\partial x_m}B_m^j\right)\right] = P_k - \beta^\star\rho k\omega \tag{3.10}$$

ω**- equation**

$$\frac{\partial(\rho\omega)}{\partial t} + \frac{1}{J}\frac{\partial}{\partial x_j}\left[(\rho\langle U_j - \dot{x_k}\rangle\beta_k^j \omega) - \frac{(\mu+\mu_t/\sigma_\omega)}{J}\left(\frac{\partial \omega}{\partial x_m}B_m^j\right)\right] = \gamma\frac{\omega}{k}P_k - \beta\rho\omega^2 + 2\rho(1-F_1)\sigma_{\omega 2}\frac{1}{\omega}\frac{\partial k}{\partial x_m}B_m^j\frac{\partial \omega}{\partial x_m}B_m^j \tag{3.11}$$

where the production of turbulent energy is expressed as :

$$P_k = 2\mu_t S_{ij}S_{ji} = \frac{\mu_t}{J^2}\left(\frac{\partial\langle U_i\rangle}{\partial x_n}\beta_j^n + \frac{\partial\langle U_j\rangle}{\partial x_m}\beta_j^n\right)\frac{\partial\langle U_i\rangle}{\partial x_n}\beta_j^n \tag{3.12}$$

$$S_{ij} \text{ is the mean strain rate} = \frac{1}{2}\left(\frac{\partial\langle U_i\rangle}{\partial x_j} + \frac{\partial\langle U_j\rangle}{\partial x_i}\right)$$

The model constants of SST model are evaluated following a linear combination of the constants used in the standard $k-\epsilon$ and the Wilcox $k-\omega$ model as $\phi = F_1\phi_1 + (1-F_1)\phi_2$, where $\phi = \sigma_k,\ \sigma_w,\ \gamma \text{ or } \beta$

The constants of set 1 (ϕ_1) are (Wilcox $k-\omega$ model) $\sigma_{k1} = 0.85$, $\sigma_{\omega 1} = 2.0$, $\beta_1 = 0.075$, $\beta^\star = 0.09$, $\kappa = 0.41$ and $\gamma_1 = \beta_1/\beta^\star - \sigma_{\omega 1}\kappa^2/\sqrt{\beta^\star}$

The constants of set 2 (ϕ_2) are (Standard $k-\epsilon$ model) $\sigma_{k2} = 1.0$, $\sigma_{\omega 2} = 0.856$, $\beta_2 = 0.0828$, $\beta^\star = 0.09$, $\kappa = 0.41$ and $\gamma_2 = \beta_2/\beta^\star - \sigma_{\omega 2}\kappa^2/\sqrt{\beta^\star}$ and the auxiliary relations are :
$F_1 = tanh(arg_1^4)$ where $arg_1 = min\left[max\left(\frac{\sqrt{k}}{0.09\omega y}; \frac{500\nu}{y^2\omega}\right); \frac{4\sigma_{\omega 2}k}{CD_{k\omega}y^2}\right]$, $F_2 = tanh(arg_2^2)$ where $arg_2 =$

$max\left(\frac{2\sqrt{k}}{0.09\omega y};\frac{500\nu}{y^2\omega}\right), CD_{k\omega} = max\left(2\rho\sigma_{\omega 2}\frac{1}{\omega}\frac{\partial k}{\partial x_m}B_m^j\frac{\partial \omega}{\partial x_m}B_m^j, 10^{-10}\right)$

Stagnation point Anomaly

The $k-\epsilon$ or SST model based on the concept of isotropic eddy viscosity usually produces an excessive level of *k* and μ_t near a stagnation point, often encountered in the vicinity of a stagnation zone. Kato and Launder [21] suggested an ad-hoc measure to replace the original production term (Eq. 3.12) by $P_k = 2\rho\mu_t|S||\Omega|$ in the k-transport equation (Eq.3.10) where $|S|$ and $|\Omega|$ are the magnitude of the mean strain rate *S* and the vorticity Ω respectively. The vorticity near stagnation zone is usually low due to almost irrotational bending of the fluid and hence the calculated values of unrealistic high level of turbulence energy may be avoided.

3.5 Numerical Solution of Finite Volume Equation

Second order accurate central difference has been used for spatial discretisation of the convective fluxes whereas the temporal derivatives are also discretised using the second order accurate three-level fully implicit scheme. Using the relevant geometric factors, appropriate discretisation schemes and linearisation of the source vector $\langle S\rangle$, the flux balance equations for momentum and turbulence scalars are expressed in an implicit manner as following :

$$\left(1.5\phi_p^{n+1} + 0.5\phi_p^{n-1} - 2\phi_p^n\right)\frac{\Delta V}{\Delta t} = \sum_{nb} A_{nb}\phi_p^{n+1} + SU - A_P\phi_P^{n+1} \tag{3.13}$$

here $A_P = \sum_{nb} A_{nb} - SP$; the coefficient A_{nb} represents the combined effect of convection and diffusion at the four faces of a computational cell denoted by the suffix *nb*; *SU* and *SP* are the components of the linearised source term $\langle S\rangle$, ΔV is the cell volume and Δt is the time step size. The superscripts of ϕ represent the respective time step. The continuity equation is also transformed to a linearised equation for pressure correction in the form of Eq. 3.13 and the corrections for pressure and velocity field obtained are added to the momentum-satisfying pressure and velocities respectively at the cell centers and cell faces. The detailed derivation of Eq. 3.13 and the iterative decoupled approach to handle the pressure-velocity link are reported by elsewhere [12, 14, 22]. The system of linearised equations (Eq. 3.13) for velocity, pressure and turbulence scalars is solved using the implicit procedure of Stone [23].

4 Results and Discussions

4.1 Turbulent flow past NACA aerofoil series

4.1.1 Motivation

Two dimensional flow simulation has been carried out for various NACA 4 digit aerofoils using the in-house code RANS3D. This analysis is carried out in order to understand the performance of these aerofoils at a relatively low chord based Reynolds number of 87000. Though the two dimensional analysis has its limitation, it is a good starting point when one needs a broader understanding of the aerodynamics and design of aerofoil sections for flight vehicles with limited computational resources. This study will be helpful to understand the aerodynamic characteristics of aerofoils at low Reynolds number that are not well understood from only limited literature available. Also the two-dimensional analysis provides a better understanding of the flow behaviour as they are free from the complex three-dimensional effects such as cross-flow and induced drag which are often difficult to discern and isolate from the computational results.

Recently published experimental and computational results [2, 3, 24] show that at low Reynolds number, the aerodynamic characteristics greatly depend on the aerofoil geometry. It is therefore important to undertake a parametric study to investigate the effect of geometrical parameters such as aerofoil thickness, camber and location of maximum camber on the aerodynamics. The major complexity at low Reynolds number is that the flow is dominated by large viscous effects which is asscociated with thick boundary layers resulting in higher viscous drag and lower maximum lift coefficient. The thickening of the boundary layer may cause the flow to undergo laminar to turbulent transition which is computationally difficult to handle. The phenomenon of transition from laminar to turbulent flow is not well understood and none of the presently available turbulence model can satisfactorily predict this complex phenomenon. However, some of the available turbulence models can be successfully employed for the comparitive study of the performance of aerofoils for different geometric parameters of interest [2, 3] and the present investigation employs the SST turbulence model [25].

4.1.2 Computational Details

For the different NACA series of aerofoils analysed, a 2-block O-grid consisting of $320 \times 100 \times 2$ control volumes has been employed with the far field placed at a radius of $15C$ and the minimum wall normal distance is maintained to be around $2 \times 10^{-4}C$, where C is the chord of the aerofoil. This grid has been fixed based on the earlier grid sensitivity study carried out by the NAL research team [26] using the RANS3D code. The typical grid for symmetric aerofoil and cambered aerofoil used for these analysis are already shown in Fig. 2.1 and Fig. 2.2 respectively. In order to accommodate the three-dimensional flow solver for the two-dimensional flow situation, only one control volume formed

by two grid nodes is considered along the span-wise direction. Symmetric boundary conditions are used at the span-wise end planes to ensure two-dimensionality of the flow. For the present study all the computations were carried out using the third order accurate QUICK [27] scheme coupled to deferred correction prodcedure [28] (*i.e.* combinig 10% of Upwind fluxes and 90 % of QUICK fluxes) for spatial discretisation scheme of convective flux. For all the aerofoil analysed the flow solution is carried out at different angle of attack (α) ranging from 0 to the stall angle. The flow is expected to be steady at smaller angles of attack and tends to become unsteady when the stall angle is approached. Keeping this in view and also in order to reduce the computation time, the flow analysis are carried out assuming the flow to be steady (*i.e* Δt is assumed to be large) for smaller angles of attack. At higher α's (approaching the stall angle) time accurate analysis are carried out using a second order accurate temporal discretisation scheme with time step size $\Delta t = 0.05$.

The typical flow boundary conditions for flow around an aerofoil is shown in Fig. 4.1 with the vertical cut boundary which divides the computation domain into two halves treated as separate blocks. The farfield is treated either as an inflow where the flow is prescribed or an outflow with convective boundary condition depending on the sign of the convective flux on the relevant face. At the aerofoil wall, the velocity components are set to zero, the convective and diffusive fluxes across the boundary are set to zero and the wall shear effect is simulated through appropriate source terms in the momentum equations. At the block (cut) boundary, one overlapping control volume is provided on the either side of the block interface boundary for appropriate transfer of the solution from the neighbouring block.

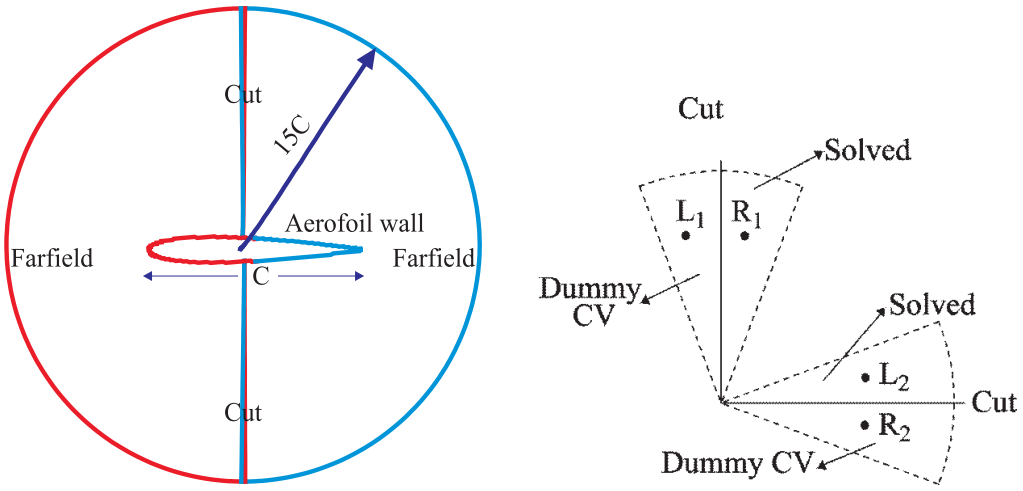

Figure 4.1: Boundary condition for multi-block flow computation

4.1.3 Effect of Reynolds number

The aerodynamic performance of the aerofoil greatly depends on the flow Reynolds number. At higher Reynolds number ($Re \geq 10^6$) the aerodynamic characteristics of the aerofoil varies marginally with the Reynolds number . However, for low Reynolds number regime ($Re \leq 10^5$), the aerodynamic

performance of the aerofoil varies rapidly as the configuration and/or Reynolds number changes. The available experimental results [24, 29] conducted in a water tunnel have shown that the aerodynamic performance of a thin flat plate is inferior to a conventional aerofoil at $Re = 1.2 \times 10^5$, but has a superior performance at $Re = 4 \times 10^4$. This indicates that the aerofoil performance is relatively poor at low Reynolds number as compared to high Reynolds numbers. The poor performance at low Reynolds number is mainly because the flow separates at a relatively low angle of attack. This laminar separation which is often formed on the upper surface of the aerofoil at low Reynolds number leads to a decrease in the performance (Lower L/D).

In order to understand the Reynolds number effect on the aerofoil performance, computations have been carried out for the flow past NACA0012 aerofoil at two Reynolds numbers; one at high Reynolds number ($Re = 10^6$) and another at low Reynolds number ($Re = 87,000$). The flow results obtained from these computations are presented in this section and compared with that of the measured values reported by NASA [30].

Fig.4.2 shows the comparision of computed surface pressure ($-C_p$) distributions over the NACA0012 aerofoil section at different angles of attack and different flow Reynolds numbers $C_p = \frac{(P-P_\infty)}{1/2\rho {U_\infty}^2}$ is the non-dimensional pressure coefficient using P_∞ and U_∞ as the freestream pressure and velocity respectively. It is clear from the figure that the predicted results for the high Reynolds number agree reasonably well with that of the experimental results confirming the adequacy of the mathematical modelling, the numerical accurancy of the RANS3D code and the turbuelnce model used for the present turbuelnt flow computation. The figure also shows that the pressure distributions for both the Reynolds numbers considered do not differ significantly for low angles of attack. However, the pressure distributions for angle of attack at 8 degree show a significant effect of Reynolds number. It was further observed that at $\alpha = 12^\circ$ the flow becomes unsteady for $Re = 87,000$ with $St = 1.182146$, whereas at $Re = 10^6$ the flow remains steady. The plot of Cp (Fig.4.2(d)) and Cf (Fig. 4.3(d)) shows the instantaneous surface pressure and skin-friction distributions respectively. For this case, the suction peak (minimum pressure) and the area enclosed by the presure distributions over the upper and lower surfaces at $Re = 10^6$ is more than that at low Reynolds number $Re = 87,000$ indicating a lift loss at the low Reynolds number due to flow separation. The chordwise variation of the computed skin friction coefficient distribution ($C_f = \frac{\tau_{wall}}{\frac{1}{2}\rho \overline{U}^2}$, where τ_{wall} is the wall shear stress) presented in Fig. 4.3 also confirms this flow separation.

The particle traces computed using the post-processing software Tecplot 9.0, from time integration of the computed velocity field for different flow conditions at $Re = 87,000$ and $Re = 10^6$ are presented in Fig. 4.4. The particle traces around the NACA0012 aerofoil section clearly show that the flow separation occurs at the low Reynolds number and it is confined to the aft portion of the upper surface of the aerofoil at $\alpha = 8^\circ$. However the instantaneous streamlines shows that ,the entire upper surface experiences a separated flow at $\alpha = 12^\circ$. This phenomenon of massive flow separation on the aerofoil upper surface at $\alpha = 12^\circ$ for $Re = 87,000$ corroborates the observations from the predicted pressure and skin friction distributions already discussed.

Reynolds No.	$(L/D)_{max}$	Stall Angle
10^6	34.05	14-15
3.6×10^6 Measurement[30]	48.49	14-15
87,000	21.80	10-12

Table 4.1: Relative performance of NACA0012 aerofoil at $Re = 10^6$ and $Re = 87,000$

The aerodynamic coefficients like the lift, drag and pitching moment can easily be computed by numerically integrating the surface forces viz., the pressure acting normal to the surface and the shear stress acting along the surface. The drag and the lift coefficients represent the resultant forces on the aerofoil in the direction of the incoming flow and its normal respectively, non-dimensionalised by the product of the dynamic head $\frac{1}{2}\rho {U_\infty}^2$ and the aerofoil chord length (C)which is the projected area of the curved aerofoil on which the surface forces act. The pitching moment is computed from the resultant force and its location with respect to the quarter chord point. The variations of the computed lift coefficient (C_l), drag coefficient (C_d) and pitching moment coefficient (C_m) with angle of attack and the drag polar are shown in Fig. 4.5 for $Re = 87,000$ and $Re = 10^6$ and compared with that of the measured data [30] available for $Re = 3.6 \times 10^6$. The agreement between the measurement data and the present computation for $Re = 10^6$ is reasonably good upto the stall angle ($\alpha \approx 14^\circ$). The small discrepancies observed in the C_l plot beyond the stall angle may be attributed partly to the uncertainty of the turbulence model used and partly to the approximations involved in the spatial and temporal discretisation of the convective flux in the present computation scheme. The variation of pitching moment (Fig. 4.5(c)) with α are observed to follow the physically expected trend (for a symmetric aerofoil the pitching moment is zero and remains constant almost up to the stall angle). The prediction also shows that the lift coefficient slope and the stall angle for the aerofoil decreases at the low Reynolds number and the drag coefficient increases. This results in the decrease of (L/D), the efficiency of the aerofoil as it is evident from the drag polar and Table 4.1

4.1.4 Effect of maximum section thickness

The effect of the maximum thickness of NACA four digit symmetric aerofoil sections has been investigated and the results obtained for different thickness (2%, 6% and 12%) are presented and discussed in this section.

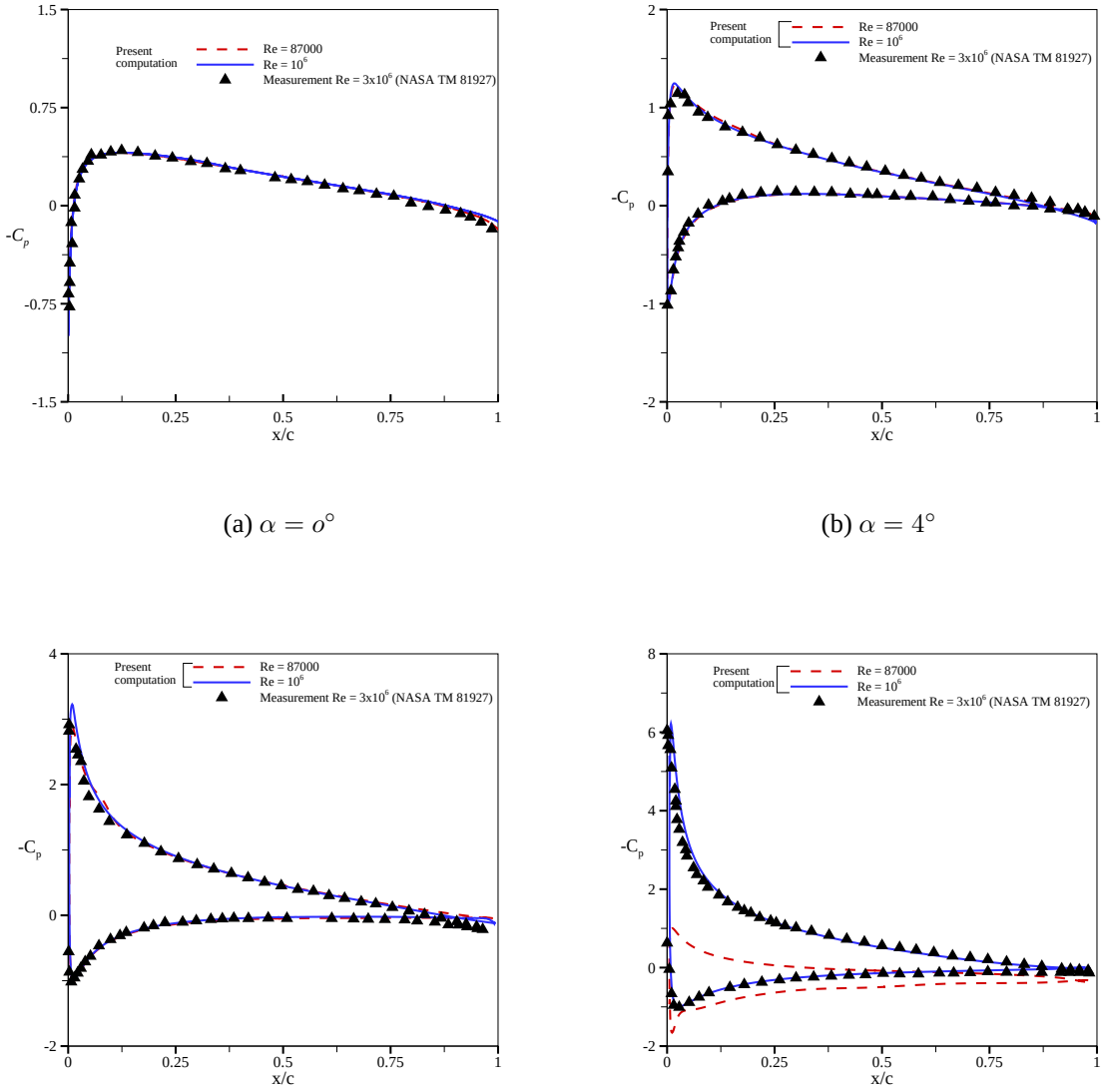

(a) $\alpha = o°$

(b) $\alpha = 4°$

(c) $\alpha = 8°$

(d) $\alpha = 12°$

Figure 4.2: Effect of Reynolds number on the chordwise variation of surface pressure for flow past NACA0012 aerofoil section at different angles of attack

The computed surface pressure ($-C_p$) distributions obtained for the three aerofoils considered are compared in Fig.4.6 at different angles of atttack (α = 0, 4 and 8 degree) for $Re = 87,000$. The pressure distributions are observed to have distinctly different slope and suction peak. At this flow Reynolds number, the aerofoil with maximum thickness has higher suction peak and also has a maximum area enclosed by the upper and lower surface of the pressure distribution as compared to the aerofoil with lesser thickness indicating a higher lift coefficeint for thicker aerofoil section. Further, the plateau-like distribution is observed for thinner aerofoil section at $\alpha = 8°$ (Fig. 4.6(c)) indicating early flow separation as evident from the computed streamlines presented in (Fig. 4.9). The formation

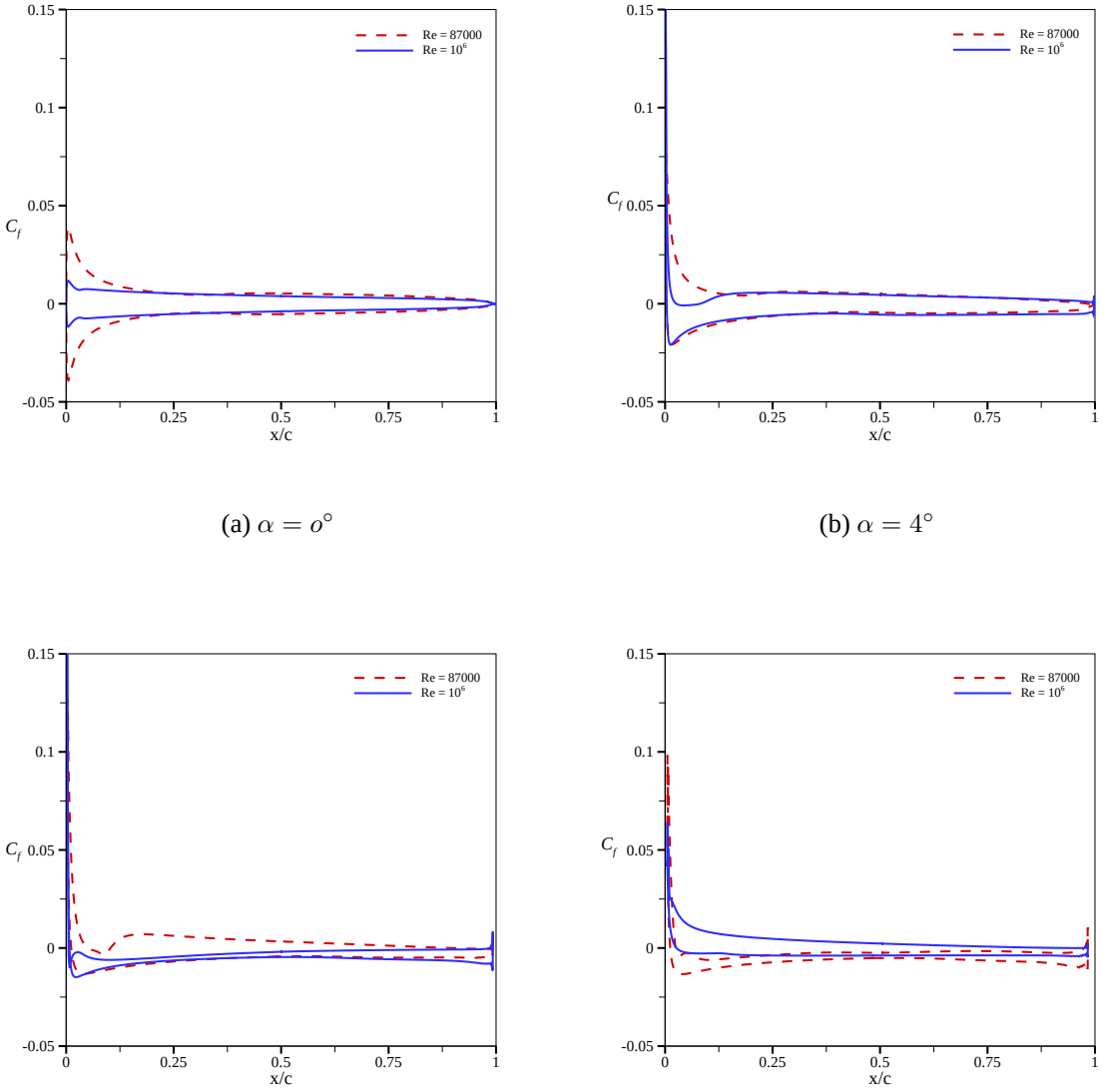

(a) $\alpha = o°$

(b) $\alpha = 4°$

(c) $\alpha = 8°$

(d) $\alpha = 12°$

Figure 4.3: Effect of Reynolds number on the chordwise variation of skin friction for flow past NACA0012 aerofoil section at different angles of attack

of early separation for thinner aerofoil section leads to a decrease in the lift coefficient.

Figs. 4.7 -4.9 shows the computed flow pattern at different angles of attack ($\alpha = 0$, 4 and 8 degree) for the three different thicknesses of the aerofoil section. For NACA0012 aerofoil section the flow remains attached upto $\alpha = 8°$, whereas for smaller thickness the flow separates at a lower angle of attack. For NACA0006 the flow seperation is observed at $\alpha = 8°$ (Fig. 4.8) and as the thickness is further reduced (NACA0002) the seperation occurs at a lower angle of attack and the separation bubble covers the entire upper surface at $\alpha = 8°$ (Fig. 4.9).

Aerofoil	$(L/D)_{max}$	Stall Angle
NACA0012	21.75	10-12
NACA0006	6.15	9-10
NACA0002	5.32	9-10

Table 4.2: Relative performance of aerofoil section with varying thickness ($Re = 87,000$)

The variation of lift coefficient (C_l), drag coefficient (C_d) and the pitching moment coefficient (C_m) with angle of attack and the drag polar obtained for the three different aerofoil sections are shown in Fig. 4.10. It is clearly evident from (Fig. 4.10) and Table 4.2, that at $Re = 87,000$, NACA0012 aerofoil seems to have better aerodynamic performance when compared to NACA0006 and NACA0002 aerofoil sections. The computed pitching moment curve (Fig. 4.10(c)) shows that for thicker aerofoil section the pitching moment remains zero upto $\alpha = 12^\circ$ whereas for the thinner aerofoil section the deviation from zero is observed at $\alpha = 4^\circ$ itself indicating that the thicker aerofoil section may be more stable at $Re = 87,000$. These computations at $Re = 87,000$ show that the aerodynamic performance of the aerofoil do not exhibit any specific trend with thickness. Hence further investigation is needed to confirm these flow features and the aerodynamic performance at this Reynolds number.

In the present study we are interested in the analysis of the aerofoil sections for MAV application. Since MAVs are very small in dimension and weighing less than 100g with the payload, most of the fixed wing MAVs use very thin aerofoil sections for their wings. Keeping this in view, the effect of camber and location of maximum camber on the aerodynamic performance is analysed only for the aerofoil with 2% thickness which are discussed in the following sub sections.

4.1.5 Effect of camber

The effect of camber for 2% thick aerofoil section with location of the camber fixed at 40% of the chord from the leading edge has been investigated for three different magnitude of camber at 2%, 4% and 6% of the chord. The flow results obtained for NACA2402, NACA4402 and NACA6402 are presented and their performance is discussed in this section

The computed surface pressure ($-C_p$) distributions obtained for the three different camber magnitudes as well as for symmetric aerofoil section (NACA0002) are compared in Fig.4.11 at different angles of atttack for $Re = 87,000$. The slope and suction peak of the pressure distribution curve is observed to vary with the variation of the camber. Also, the flow pattern obtained (Fig. 4.12-4.14)

Aerofoil	$(L/D)_{max}$	Stall Angle
NACA0002	5.32	9-10
NACA2402	8.77	8-10
NACA4402	13.00	8-10
NACA6402	19.64	8-10

Table 4.3: Relative performance of 2% thick NACA aerofoil section with varying camber ($Re = 87,000$)

with varying camber is observed to be distinctly different with NACA6402 having a smoother flow compared to the other two aerofoil sections (NACA2402 and NACA4402).

The variation of lift coefficient (C_l), drag coefficient (C_d) and the pitching moment coefficient (C_m) with angle of attack and the drag polar obtained for the three different aerofoil sections are shown in Fig. 4.15. The variation of pitching moment (4.15(c)) with α is observed to follow the physically expected trend (for a cambered aerofoil the pitching moment is non-zero and remains constant almost up to the stall angle). It is clearly evident from the drag polar curve (Fig. 4.15(d)) and Table 4.3, that at $Re = 87,000$ the aerofoil section with higher camber seems to have better aerodynamic performance when compared to aerofoil section with lower camber. This corroborates with the increased smoothness of the flow for NACA6402 compared to NACA4402 and NACA2402.

4.1.6 Effect of maximum camber location

The effect of maximum camber location for 2 % thick aerofoil section with 4% camber are investigated for three different camber locations at 20%, 40% and 60% of the chord measured from the leading edge of the aerofoil. The flow results obtained for NACA4202, NACA4402 and NACA4602 are presented and their relative performance is discussed in this section.

The computed surface pressure ($-C_p$) obtained for the three different maximum camber location is compared in Fig.4.16 at different angles of attack for $Re = 87,000$. The pressure distribution curves for various maximum camber locations are observed to have different slopes and suction peaks. The computed flow patterns for different maximum camber locations are shown in Figs. 4.17, 4.13,4.18.

The variation of lift coefficient (C_l), drag coefficient (C_d), the pitching moment coefficient (C_m) with angle of attack and the drag polar obtained for the three different aerofoil sections are shown in

Aerofoil	$(L/D)_{max}$	Stall Angle
NACA4202	22.31	8-10
NACA4402	13.00	8-10
NACA4602	11.03	8-10

Table 4.4: Relative performance of 2% thick and 4% camber aerofoil sections with varying the location of maximum camber ($Re = 87,000$)

Fig. 4.19. It is clearly evident from the drag polar (Fig. 4.19(d)) and Table 4.4, that at $Re = 87,000$ the aerodynmaic performance of the aerofoil section depends on the location of the maximum camber. The NACA4202 is observed to have significantly higher $(L/D)_{max}$ as compared to NACA4402 and NACA4602 indicating that NACA4202 may be a good choice when the flow Reynolds number is 87,000.

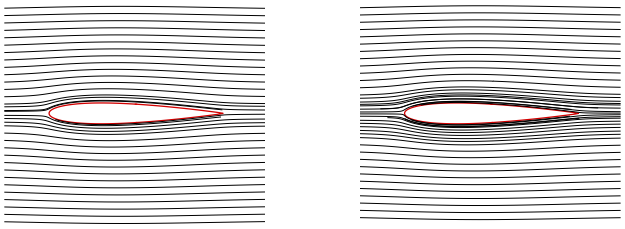

(a) $\alpha = o^{\circ}$

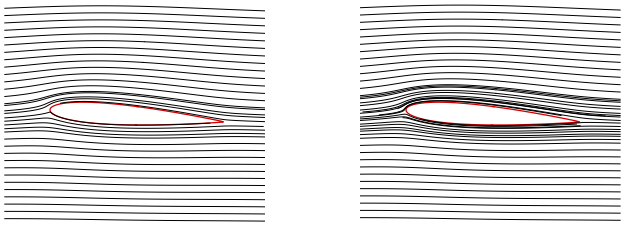

(b) $\alpha = 4^{\circ}$

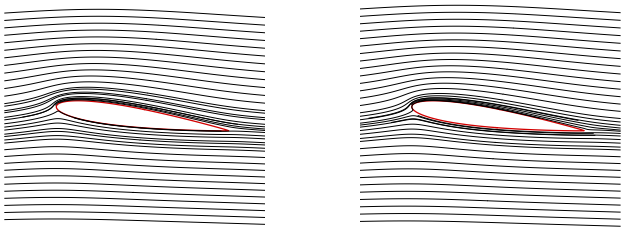

(c) $\alpha = 8^{\circ}$

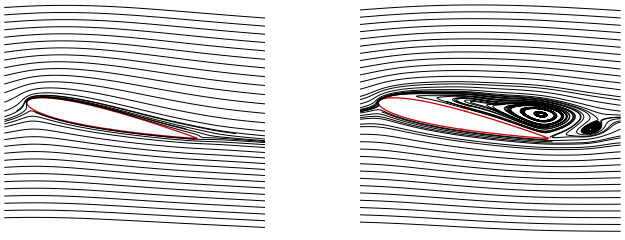

(d) $\alpha = 12^{\circ}$

$Re = 10^6$ $Re = 87,000$

Figure 4.4: Computed streamlines for flow past NACA0012 aerofoil section at different angles of attack for $Re = 10^6$ and $Re = 87,000$

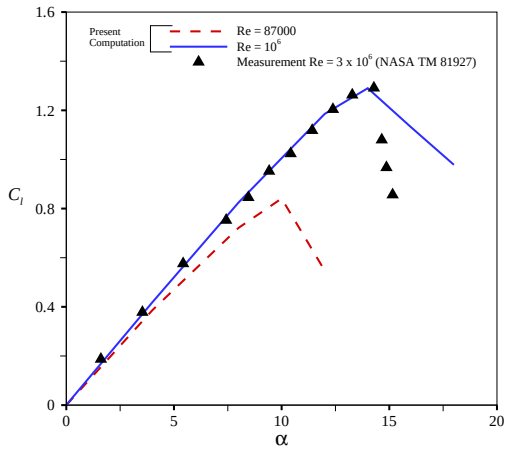

(a) Coefficient of lift (C_l)

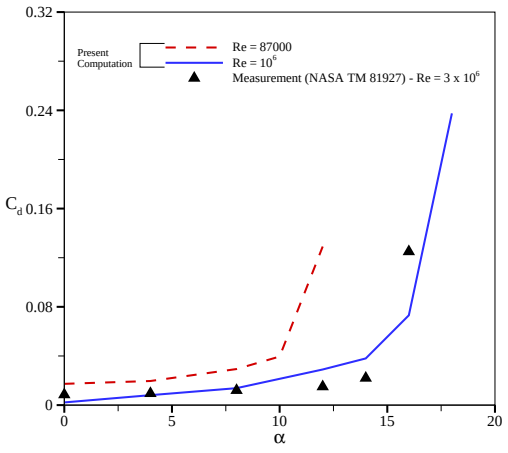

(b) Coefficient of drag (C_d)

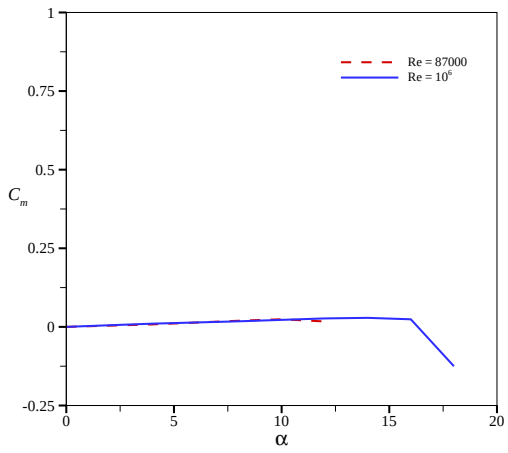

(c) Coefficient of moment (C_m)

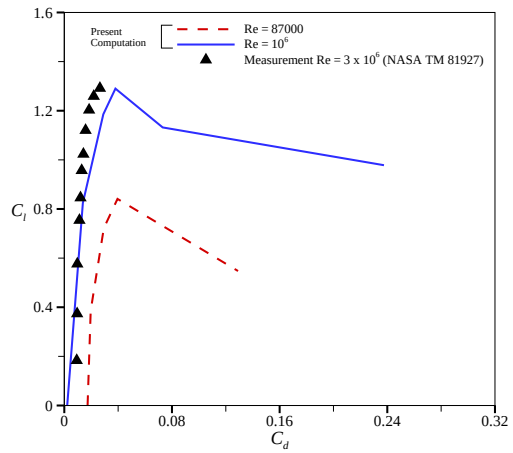

(d) Drag polar

Figure 4.5: Variation of different aerodynamic coefficients for turbulent flow past NACA0012 aerofoil section for $Re = 10^6$ and $Re = 87,000$

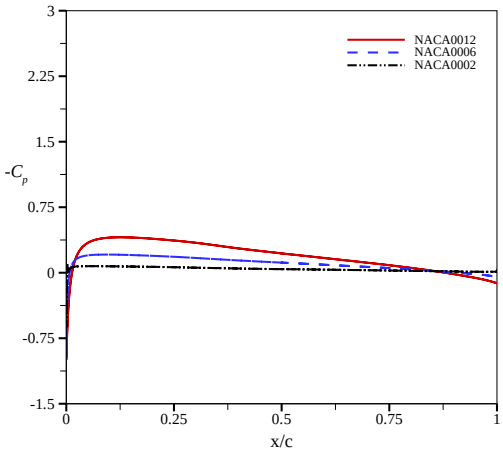

(a) $\alpha = o°$

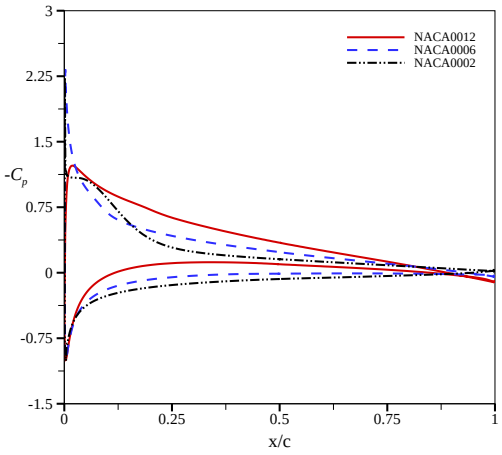

(b) $\alpha = 4°$

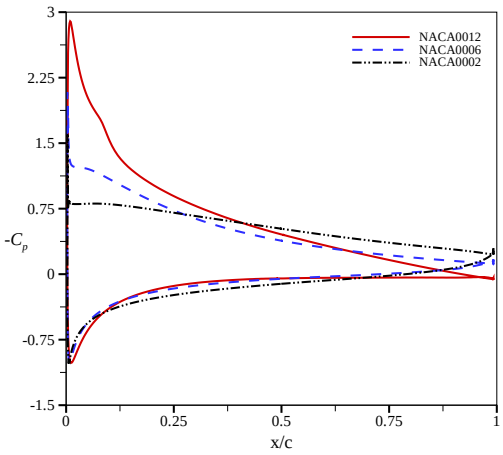

(c) $\alpha = 8°$

Figure 4.6: Chordwise variation of surface pressure for flow past symmetric NACA aerofoil section with varying thickness at different angles of attack

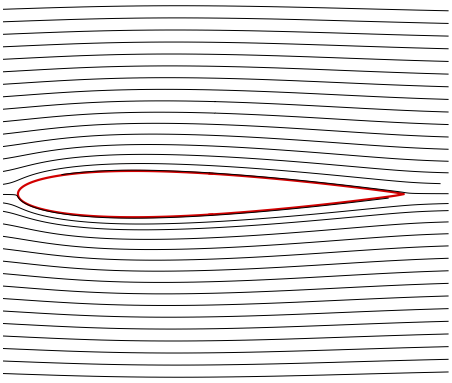

(a) $\alpha = o^{\circ}$

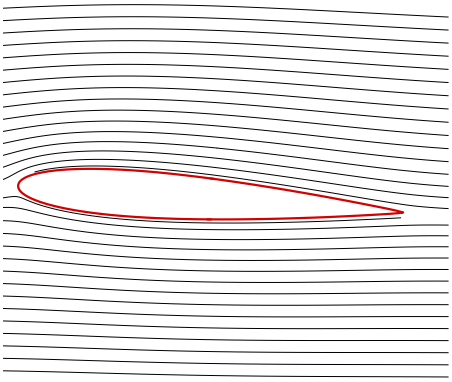

(b) $\alpha = 4^{\circ}$

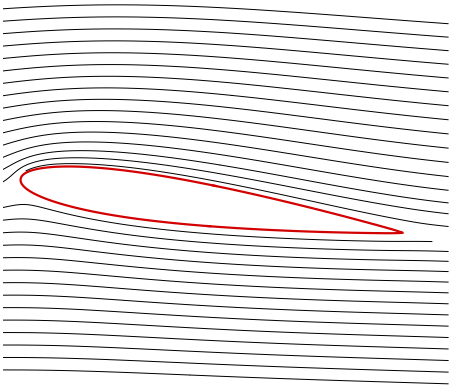

(c) $\alpha = 8^{\circ}$

Figure 4.7: Computed streamlines for flow past NACA0012 aerofoil section at different angles of attack for $Re = 87,000$

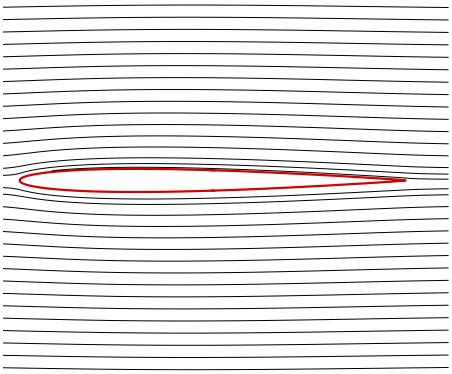

(a) $\alpha = o^{\circ}$

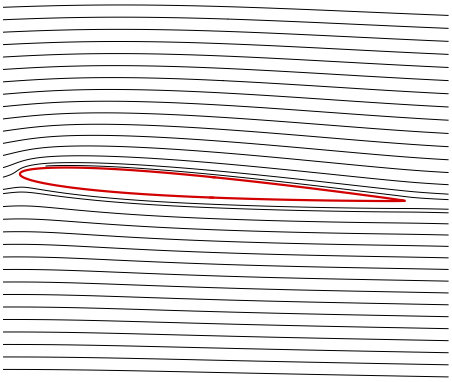

(b) $\alpha = 4^{\circ}$

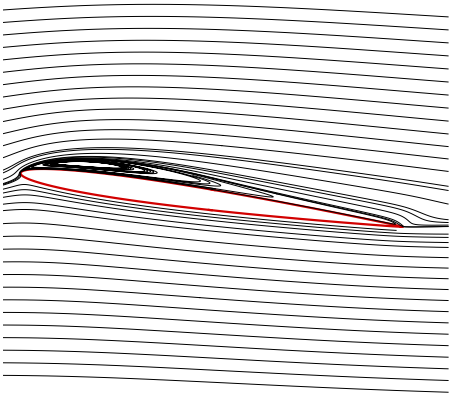

(c) $\alpha = 8^{\circ}$

Figure 4.8: Computed streamlines for flow past NACA0006 aerofoil section at different angles of attack for $Re = 87,000$

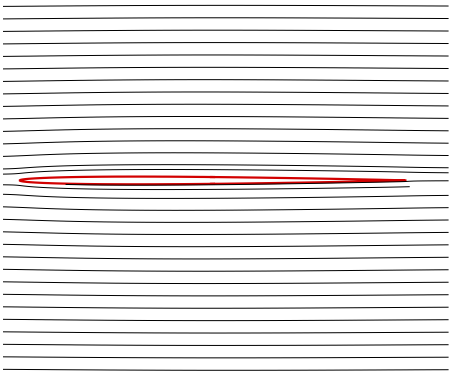

(a) $\alpha = o^{\circ}$

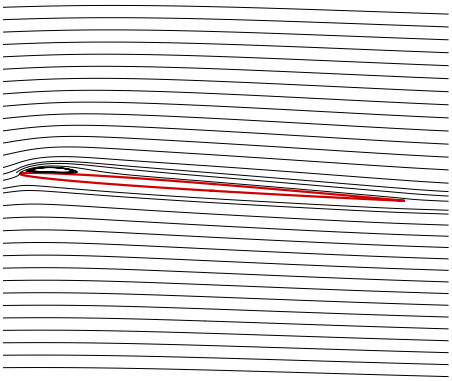

(b) $\alpha = 4^{\circ}$

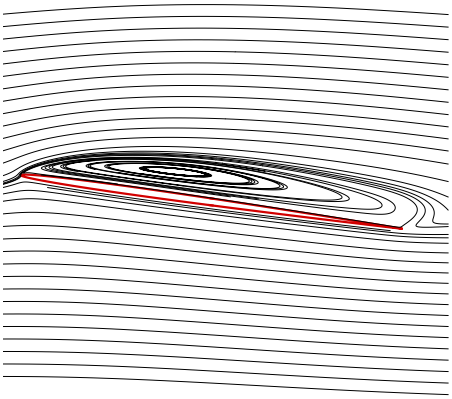

(c) $\alpha = 8^{\circ}$

Figure 4.9: Computed streamlines for flow past NACA0002 aerofoil section at different angles of attack for $Re = 87,000$

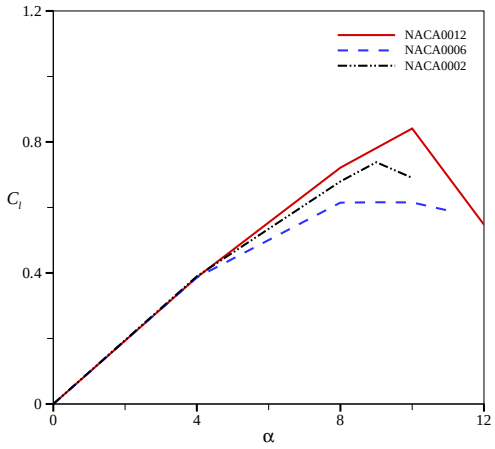

(a) Coefficient of lift (C_l)

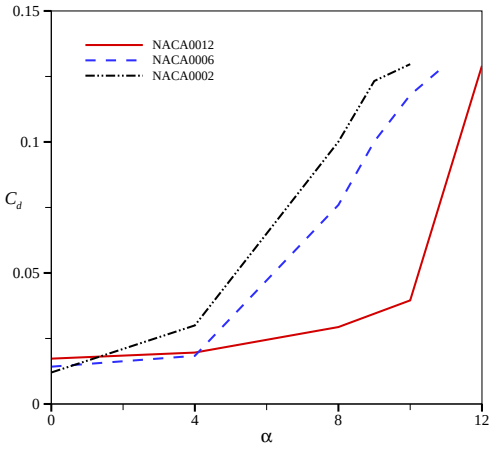

(b) Coefficient of drag (C_d)

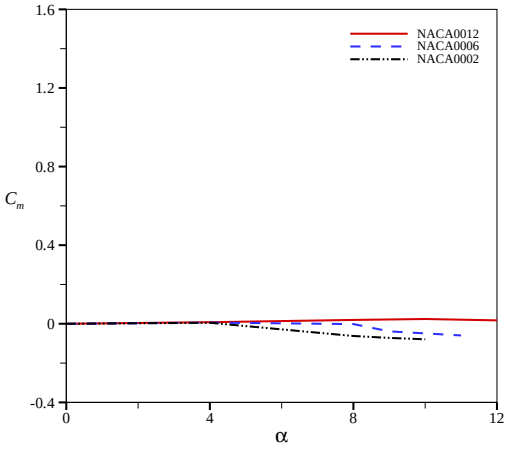

(c) Coefficient of moment (C_m)

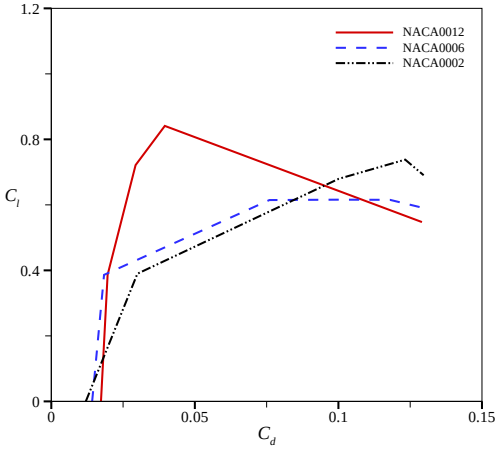

(d) Drag polar

Figure 4.10: Variation of different aerodynamic coefficients for turbulent flow past symmetric NACA aerofoil section with different thickness

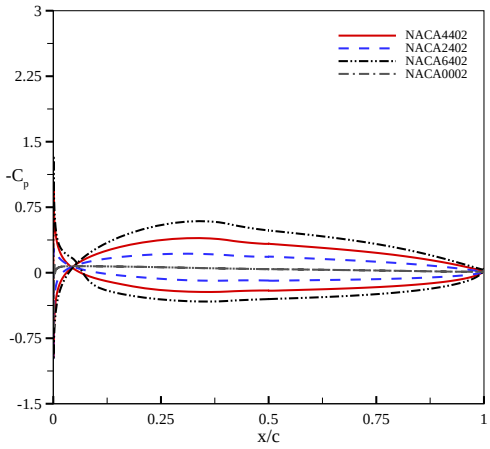

(a) $\alpha = o°$

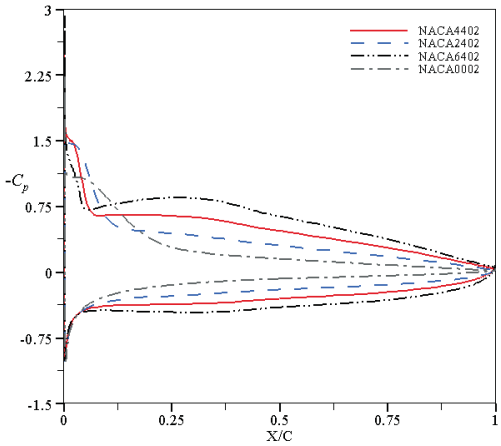

(b) $\alpha = 4°$

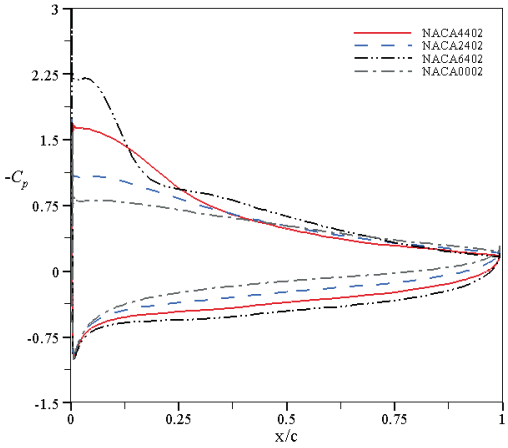

(c) $\alpha = 8°$

Figure 4.11: Chordwise variation of surface pressure for flow past NACA aerofoil section with varying camber at different angles of attack

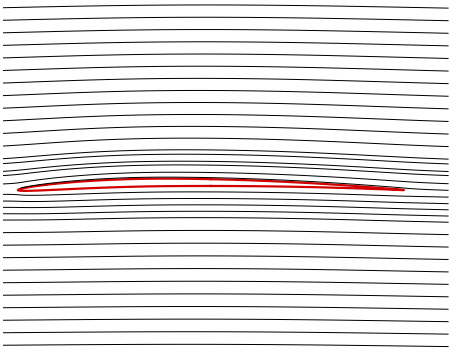

(a) $\alpha = o^{\circ}$

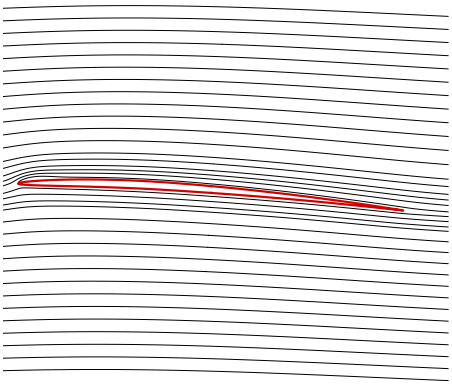

(b) $\alpha = 4^{\circ}$

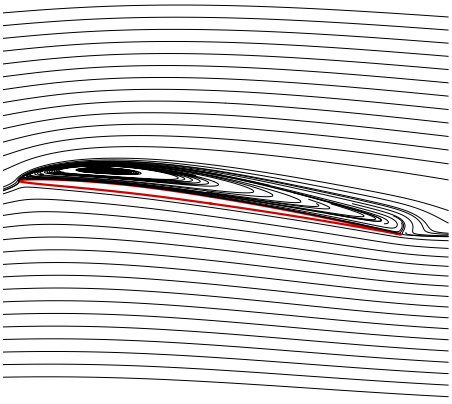

(c) $\alpha = 8^{\circ}$

Figure 4.12: Computed streamlines for flow past NACA2402 aerofoil section at different angles of attack for $Re = 87,000$

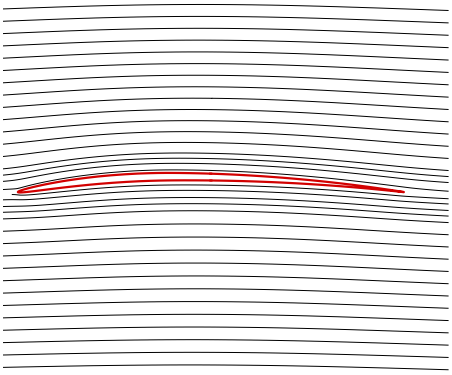

(a) $\alpha = o^{\circ}$

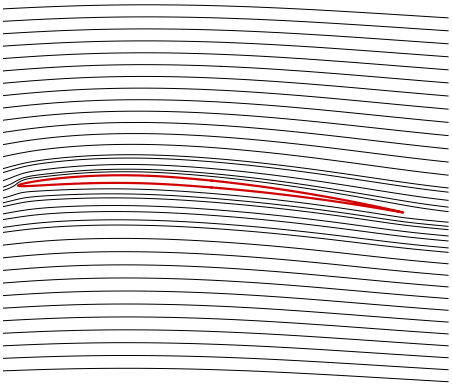

(b) $\alpha = 4^{\circ}$

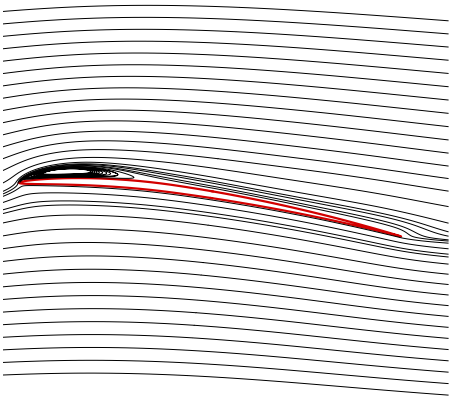

(c) $\alpha = 8^{\circ}$

Figure 4.13: Computed streamlines for flow past NACA4402 aerofoil section at different angles of attack for $Re = 87,000$

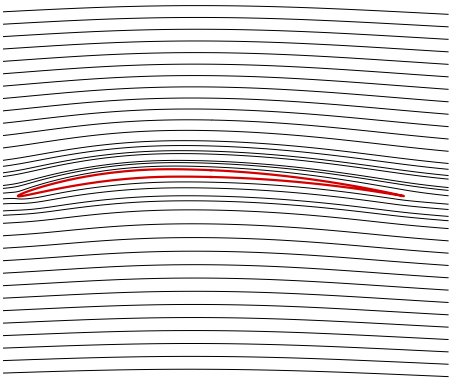

(a) $\alpha = o^{\circ}$

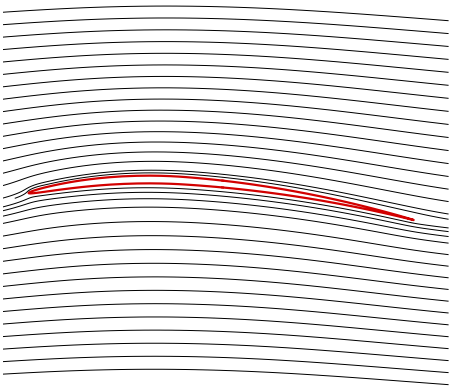

(b) $\alpha = 4^{\circ}$

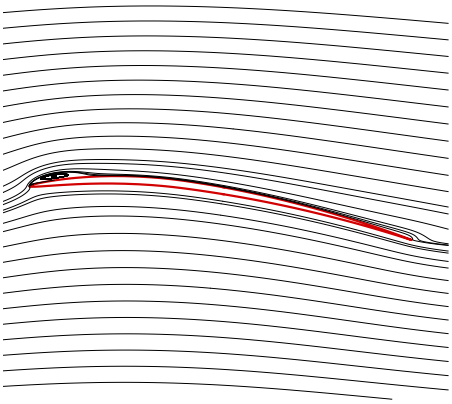

(c) $\alpha = 8^{\circ}$

Figure 4.14: Computed streamlines for flow past NACA6402 aerofoil section at different angles of attack for $Re = 87,000$

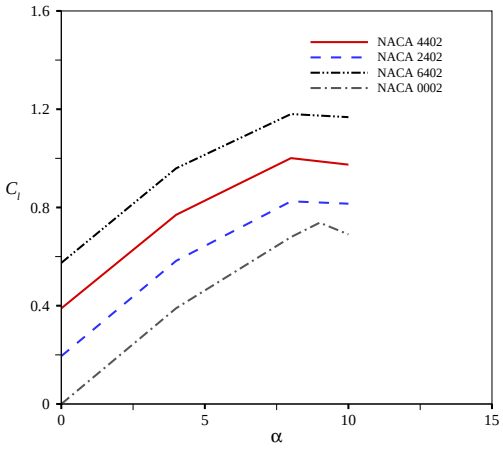

(a) Coefficient of lift (C_l)

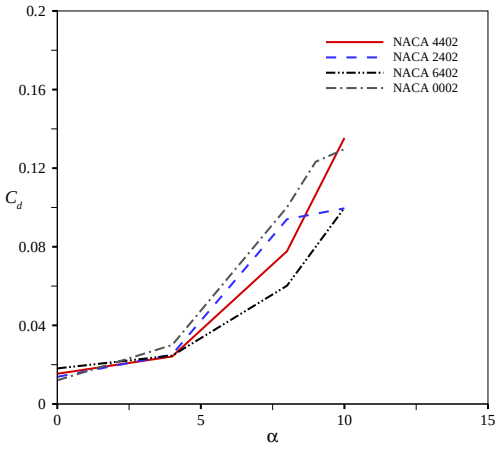

(b) Coefficient of drag (C_d)

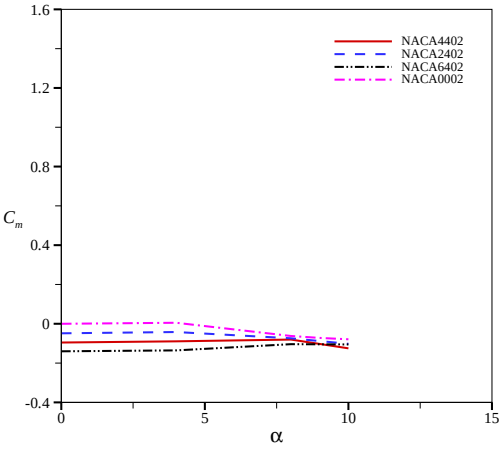

(c) Coefficient of moment (C_m)

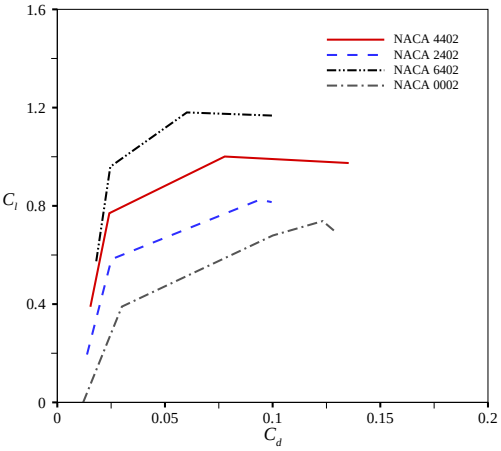

(d) Drag polar

Figure 4.15: Variation of different aerodynamic coefficients for turbulent flow past NACA aerofoil section with different camber

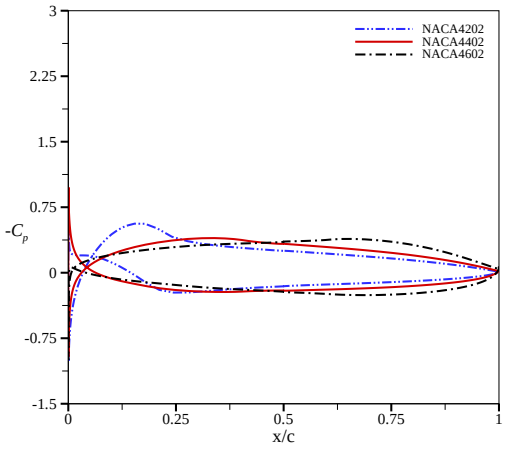

(a) $\alpha = o^\circ$

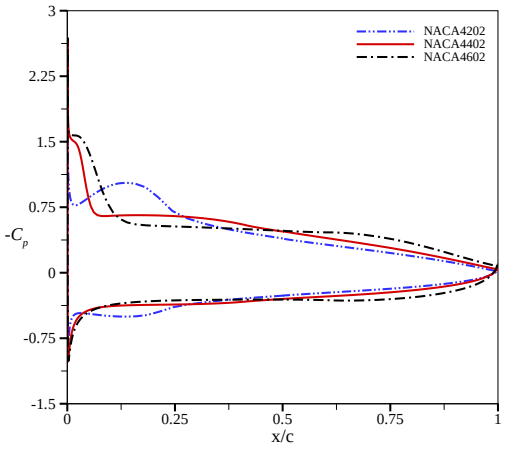

(b) $\alpha = 4^\circ$

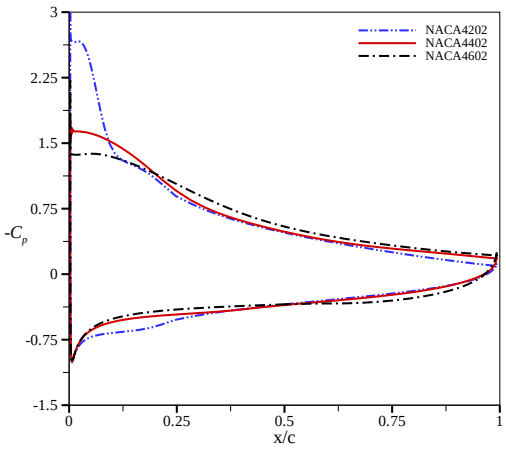

(c) $\alpha = 8^\circ$

Figure 4.16: Chordwise variation of surface pressure for flow past NACA aerofoil section with varying location of maximum camber at different angles of attack

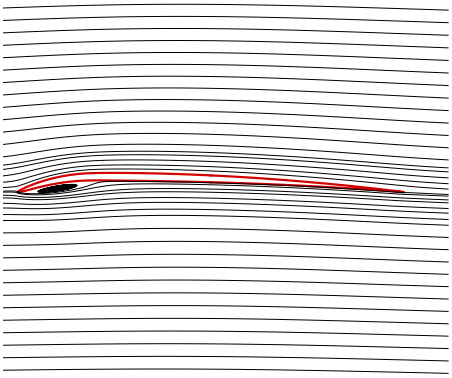

(a) $\alpha = o^{\circ}$

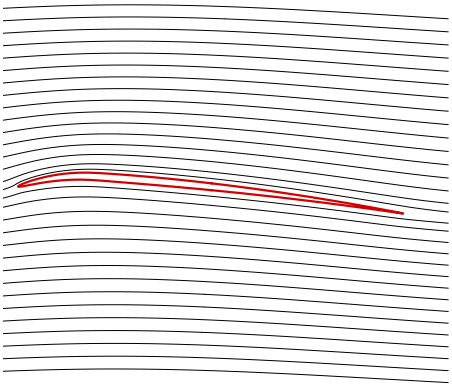

(b) $\alpha = 4^{\circ}$

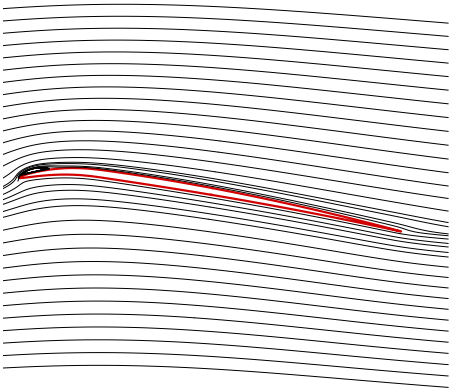

(c) $\alpha = 8^{\circ}$

Figure 4.17: Computed streamlines for flow past NACA4202 aerofoil section at different angles of attack for $Re = 87,000$

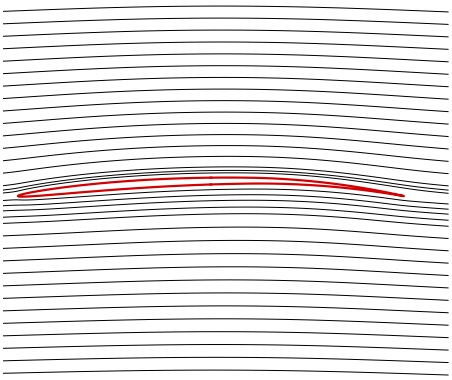

(a) $\alpha = o^{\circ}$

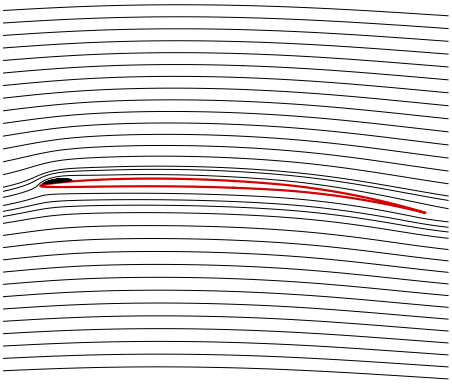

(b) $\alpha = 4^{\circ}$

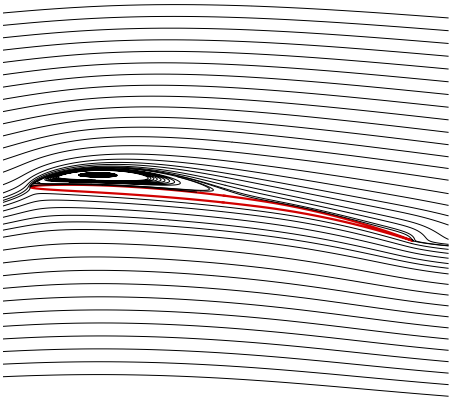

(c) $\alpha = 8^{\circ}$

Figure 4.18: Computed streamlines for flow past NACA4602 aerofoil section at different angles of attack for $Re = 87,000$

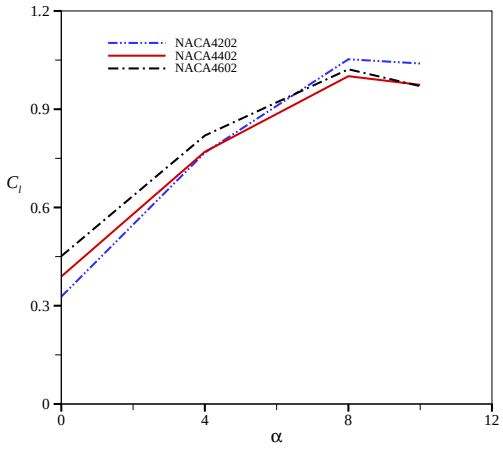

(a) Coefficient of lift (C_l)

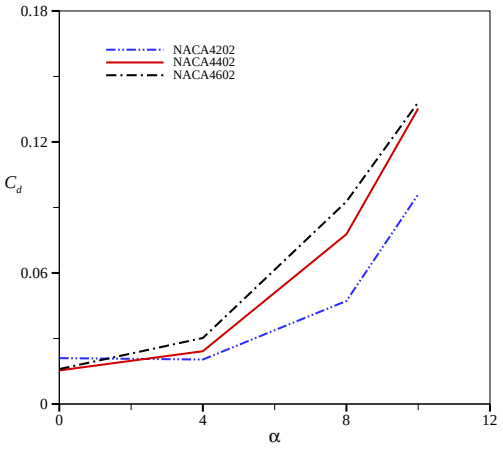

(b) Coefficient of drag (C_d)

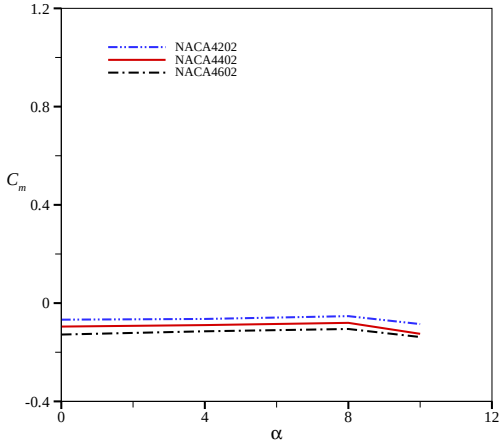

(c) Coefficient of moment (C_m)

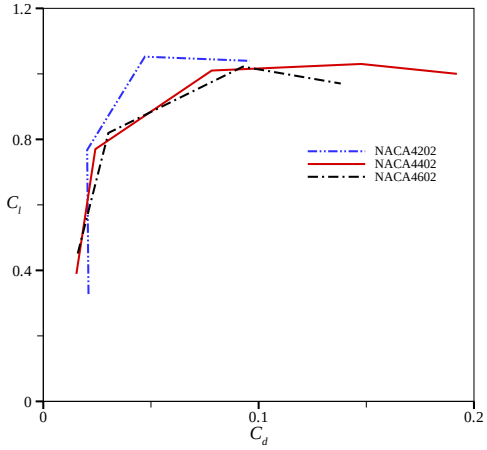

(d) Drag polar

Figure 4.19: Variation of different aerodynamic coefficients for turbulent flow past aerofoil section with different maximum camber location

5 Concluding Remarks

The NAL-RANS3D code has been successfully used to generate multiblock curvilinear structured grid around symmetric as well as cambered aerofoil sections with specified control of near wall resolution.

The RANS3D flow solution code has been run successfully for turbulent flow past different 4-digits NACA series aerofoil section at a chord based Reynolds number of 87,000 for different angles of attack. The present analysis uses the third order accurate QUICK scheme for convective flux discretisation and SST model to simulate the effect of turbulence.

The relative performance of different NACA series aerofoil sections are assessed by comparing their surface pressure distribution, skin friction distribution, flow pattern, variation of aerodynamic coefficients with angle of attack and the drag polar curve.

Reasonable agreement between the present prediction and the experimental data [30] for Coefficient of pressure and aerodynamic coefficients for the flow past NACA 0012 aerofoil at $Re = 10^6$ demonstrate the adequacy and robustness of the present flow solution algorithm RANS3D and the turbulence model used.

The present analysis has shown that (a) the NACA0012 aerofoil section has significantly better aerodynamic performace at $Re = 10^6$ as compared to $Re = 87,000$, *i.e.* at higher Reynolds number the NACA0012 has larger lift to drag ratio with delayed stall angle. (b) At $Re = 87,000$ NACA0012 has better aerodynamic performance than the symmetric aerofoil with lesser thickness (NACA0006 and NACA0002). (c) the results obtained for the aerodynamic performance for different camber and location of maximum camber for 2% thick aerofoil section shows that larger the camber and closer the location of maximum camber to the leading edge better is the lift to drag ratio for $Re = 87,000$. From the present analysis we may conclude that the choice of NACA4202 aerofoil section is beneficial for MAV wing. The present trend also indicates that NACA6202 aerofoil section may also be a good choice which will have to be confirmed through further investigation.

In future, advanced turbulence models with appropriate modeling of laminar to turbulent transition in the present eddy viscosity framework may be incorporated in the RANS3D code to generate more accurate results for the low Reynolds number regime.

References

[1] J. M. Grameyer and M. T. Keennon. Development of the black Mirco Air Vehicle. *AIAA Paper*, 2001-0127, 2001.

[2] P. J. Kunz. Aerodynamics and design for ultra-low Reynolds number flight . *PhD Dissertation, Stanford University, US*, 2003.

[3] E. J. Schroeder. Low Reynolds number flow validation using Computational Fluid Dynamics with application to Micro Air Vehicles. *Master of Science Dissertation, Dept. of Aerospace Engineering, University of Maryland, US*, 2005.

[4] G. W. Jones, C. J. Bradshaw, J. Papadapoulos, and M. F. Paltzer. Improved performace and control of flapping-wing propelled Micro Air Vehicles. *AIAA Paper*, 2004-0399, 2004.

[5] W. Shyy, M. Berg, and D. Ljungqvist. Flapping and flexible wings for biological and micro vehicles. *Progress in Aerospace Sciences*, 35(5):455–506, 1999.

[6] Y. Lian and W. Shyy. Laminar-turbulent transition of low Reynolds number rigid or flexible airfoil. *AIAA Journal*, 45(7):1501–1513, 2007.

[7] P. J. Kunz and R. C. Strawn. Analysis and design of rotors at Ultra-low Reynolds number . 40^{th} *AIAA Aerospace Meeting and Exhibit, Reno, NV, January*, 2002.

[8] F. Bohorquez, F. Rankins, F. Baeder, and D. J. Pines. Hover performance of rotor blades at low Reynolds number for rotary wing Micro Air Vehicles. An Experimental and CFD study . 21^{st} *AIAA Applied Aerodynamics Conference, Orlando, FL, June*, 2003.

[9] B. R. Hein. Hover performance of a Micro Air Vehicle: Rotors at low Reynolds number. *AHS Lichten Award Competition*, 2005.

[10] T. J. Mueller. Aerodynamic mesurement of low Reynolds number for fixed wing Micro-Air Vehicle. *VKI, Belgium, September 13-17*, 1999.

[11] S. Majumdar. Pressure based Navier Stokes solver for three-dimensional flow in hydrodynamics and low speed aerodynamics application . *Proc.* 3^{rd} *Asian CFD Conference, Bangalore*, 1:137–146, 1998.

[12] S. Majumdar, W. Rodi, and J. Zhu. Three dimensional finite volume method for incompressible flows with complex boundaries. *Journal of Fluid Engineering, ASME*, :496–503, 1992.

[13] S. Majumdar and B. N. Rajani. Numerical computation of flow around aerostats using a pressure-based Navier-Stokes solver. *Journal of Aeronautical Society of India*, 53(2):117–127, 2001.

[14] S. Majumdar, B. N. Rajani, D. S. Kulkarni, and S. Mohan. RANS computation of low speed turbulent flow in complex configuration. *Proc. Symposium on State of the Art and Future Trends of CFD at NAL, NAL SP03*, 01:31–48, 2003.

[15] A. Fathima, N. S. Baldawa, S. Pal, and S. Majumdar. Grid generation for arbitrary 2D configurations using a differential algebraic hybrid method . *NAL PD CF 9461*, 1994.

[16] J. Zhu. A hybrid differential-algebraic method for three dimensional grid generation. *International Journal of Numerical Methods in Engineering*, 29:1271–1279, 1990.

[17] T. Cebeci and A. M. O Smith. Analysis of turbulent boundary layers. *Academic Press, NY*, 1974.

[18] B. S. Baldwin and H. Lomax. Thin layer approximation and algebraic model for separated turbulent flows. *AIAA Paper*, 78:257, 1978.

[19] D. C. Wilcox. *Turbulence modeling for CFD*. DCW Industries Inc. California, 1993.

[20] B. E. Launder and D. B. Spalding. The numerical computation of turbulent flows. *Computer Methods and Applied Mechanics and Engg.*, 3:269, 1974.

[21] M. Kato and B. E. Launder. The modelling of turbulent flow around stationary and vibrating cylinder. *Proc. 9th Symposium Turbulent shear flows, Kyoto*, 1993.

[22] B. N. Rajani. Numerical simulation of laminar flow past a circular cylinder. *Research Progress Report 1 Submitted to NITK Surathkal*, 2007.

[23] H. L. Stone. Iterative solution of implicit approximations of multidimensional partial differential equations. *SIAM Journal of Numerical Analysis*, 5:530–530, 1968.

[24] R. T. Jones. *Wing Theory*. Princeton University Press, 1990.

[25] F. R. Menter. Two-equation eddy-viscosity turbulence models for engineering application . *AIAA J*, 32:269–289, 1994.

[26] D. S. Kulkarni, B. N. Rajani, and S. Majumdar. RANS computation of turbulent flow around aerofoils using $k - \epsilon$ turbulence model. *NAL PD CF 0212*, 2002.

[27] B. P. Leonard. A stable and accurate convective modelling procedure based on quadratic interpolation. *Computers Methods in Applied Mechanics and Engg.*, 19:59–98, 1979.

[28] P. K. Khosla and S. G. Rubin. A diagonally dominant second-order accurate implicit scheme. *Computers and Fluids*, 2:207–209, 1974.

[29] S. Sunada, A. Sakaguchi, and K. Kawachi. Aifoil section characteristics at low Reynolds number. *Trans. ASME: J Fluids Engineering*, 119:129–135, 1968.

[30] Charles D. Harris. Two-dimesnional aerodynamic characteristics of the NACA0012 airfoil in the Langley 8-Foot transonic pressure tunnel. *NASA Technical Memorandum 81927, April*, 1981.